

Statistical detection and imaging of objects hidden in turbid media using ballistic photons

Sina Farsiu,^{1,*} James Christofferson,² Brian Eriksson,³ Peyman Milanfar,² Benjamin Friedlander,² Ali Shakouri,² and Robert Nowak³

¹Eye Research Center, Duke University, Durham, North Carolina 27710, USA

²Electrical Engineering Department, University of California, Santa Cruz, California 95064, USA

³Electrical Engineering Department, University of Wisconsin-Madison, Madison, Wisconsin 53706, USA

*Corresponding author: sina.farsiu@duke.edu

Received 12 February 2007; revised 27 June 2007; accepted 24 June 2007;
posted 28 June 2007 (Doc. ID 79987); published 9 August 2007

We exploit recent advances in active high-resolution imaging through scattering media with ballistic photons. We derive the fundamental limits on the accuracy of the estimated parameters of a mathematical model that describes such an imaging scenario and compare the performance of ballistic and conventional imaging systems. This model is later used to derive optimal single-pixel statistical tests for detecting objects hidden in turbid media. To improve the detection rate of the aforementioned single-pixel detectors, we develop a multiscale algorithm based on the generalized likelihood ratio test framework. Moreover, considering the effect of diffraction, we derive a lower bound on the achievable spatial resolution of the proposed imaging systems. Furthermore, we present the first experimental ballistic scanner that directly takes advantage of novel adaptive sampling and reconstruction techniques. © 2007 Optical Society of America
OCIS codes: 100.0100, 030.6600, 140.0140, 320.0320.

1. Introduction

High-resolution imaging and detection of objects hidden in a turbid (scattering) medium have long been challenging and important problems with many industrial, military, and medical applications. Although turbid media such as fog, smoke, haze, or body tissue are virtually transparent to radar range electromagnetic waves, the resolution of radar-based imaging systems is often insufficient for many practical applications. Moreover, in some instances the transparency characteristics of certain objects (targets) and the medium are very close in the radar range spectrum, making them practically indistinguishable from each other. On the other hand, although the resolution of imaging systems using ultrashort wavelengths (e.g., x rays) is desirable, there exist potential health hazards for imaging subjects and technicians alike.

As an alternative, imaging systems working in the optical-infrared spectrum range (laser scanners) are

potentially able to produce high-resolution images without the likely health hazards. Unfortunately, even a very thin and powerful collimated laser beam quickly diffuses as it travels in turbid media, similar to a car's headlights in fog. Therefore, a naive approach to optical imaging of objects hidden inside a turbid medium results in blurry images where targets are often indistinguishable from each other or the background.

Fortunately, the advent of the new tunable solid-state lasers and ultrafast optical detectors has enabled us to acquire high-quality images through turbid media where the resolution is only limited by diffraction. Although many efficient imaging systems for capturing high-resolution images through turbid media have been proposed throughout the years [1], in this paper we mainly focus on ultrafast time-gated or coherent imaging systems [2]. We note that the proposed methods and analysis are valid and applicable for a great range of imaging systems including optical coherence tomography [3] and x-ray imaging systems.

Ultrafast time-gated imaging is based on scanning the region of interest (ROI) point by point by sending

fast bursts of optical energy (laser pulses) and detecting the unscattered (coherent) photons that have passed through the medium or reflected from the object. Although most of the photons in a laser pulse are either randomly scattered (losing their coherence) or absorbed as they travel through turbid media, across short distances, a few photons keep their coherence and pass through in straight lines without being scattered. These coherent photons are commonly referred to as the ballistic photons. Aside from the diffusive and ballistic photons, the photons that are slightly scattered, retaining some degree of coherence, are referred to as snake photons.

In what follows in this paper, we focus on studying and improving the performance of ballistic imaging systems. In Section 2, we describe a statistical model for the signal and noise in a typical ballistic imaging scenario. Furthermore, we describe optimal methods for characterizing the optical properties of the scattering medium and the semitransparent objects inside it. In Section 3, we study the performance limits of optimal single-pixel detection systems. Moreover, we show that better detection rates are achievable using a multipixel detection technique based on the generalized likelihood ratio test (GLRT) principle. The effect of diffraction on the detection rate is discussed in Section 4. In Section 5, we describe a laboratory setup for detecting ballistic photons and capturing high-resolution images through turbid media, where real experimental data are presented to further clarify the concept of ballistic imaging. In Subsection 5.B, we describe an adaptive sampling scheme that effectively reduces the image acquisition time, making ballistic imaging more suitable for practical applications. A summary and future work directions are given in Section 6, which concludes this paper.

2. Statistical Model for Ballistic Imaging Systems

To have a better understanding of the practical issues involved in photon-limited imaging via ballistic systems, let us consider the imaging system described by Zevallos *et al.* [4] where the pumped Ti:sapphire laser radiates 800 nm pulses at a repetition rate of 1 kHz and an average power of 60 mW. It is easy to show that the energy delivered by the laser during each pulse is

$$e_{\text{pulse}} = \frac{60 \times 10^{-3} \times 1 \text{ s}}{1000} = 6 \times 10^{-5} \text{ J},$$

and the energy of each photon is computed as

$$e = hf = \frac{hc}{\Lambda} = 2.4830 \times 10^{-19} \text{ J},$$

where $h = 6.626 \times 10^{-34}$ is Planck's constant, $c = 299,792,458$ m/s is the speed of light, and $\Lambda = 800$ nm is the wavelength. Now the number of photons in each packet of energy (pulse) is easily

computed as

$$I_0 = \frac{6 \times 10^{-5}}{2.4830 \times 10^{-19}} = 2.4164 \times 10^{14} \text{ photons.} \quad (1)$$

Because of the statistical nature of pulse propagation, as a laser beam travels through a diffusive medium, it is possible that some of the photons emerge without being scattered. By selecting these unscattered ballistic photons and rejecting the scattered (diffused) ones, it is possible to obtain nonblurred images that are the sharp shadows of targets buried in the diffusive medium.

Since the diffusive and ballistic photons have different path lengths, a femtosecond laser pulse generator and an ultrafast time gate can be paired to separate the relatively slow (delayed) diffusive photons from the ballistic ones. We will say more on a practical setup of a ballistic photon imaging system in Section 5. In what follows in this section, we focus on modeling the detected ballistic photons and noise from a statistical point of view.

A. Modeling Received Signal Power

As expected, in relatively long distances, the number of detected ballistic photons is extremely small. Indeed, Beer's law [5] dictates an exponential relationship between the intensity of the transmitted light and that of the ballistic component as

$$I_b = I_0 \exp\left(-\frac{d}{L}\right). \quad (2)$$

In this expression, I_0 is the number of the generated photons in one laser pulse before entering the turbid medium, I_b is the number of the ballistic photons that survive traveling through the medium, d is the distance traveled through the medium, $L = 1/\mu_t$ is the mean free path (MFP) length (average distance photons travel before being scattered), and $\mu_t = \mu_s + \mu_a$ is the medium extinction factor (the summation of scattering and absorptive coefficients, respectively). From Eqs. (1) and (2), it is clear that for the laboratory imaging systems with laser power of the order of the one described by Zevallos *et al.* [4], it is fairly unlikely that any ballistic photon survives imaging scenarios where the ratio of d/L is larger than ~ 30 MFPs. In Appendix A, we have included a detailed decision-theoretic study for defining the critical distance after which the conventional (non-time-gated) imaging systems are preferred to the time-gated ballistic systems.

The exponential drop in the number of received photons is the main prohibitive factor for using such high-resolution optical imaging systems across long distances. In such imaging scenarios, we are forced to rely on the less immediately informative (due to the inherently severe blur) snake and diffusive photons. In recent literature [6,7], an accurate yet computationally manageable mathematical model for diffu-

sive light propagation in turbid media is presented. Cai *et al.* [8] analyzed and experimented on such an imaging modality and Das *et al.* [9] and Gibson *et al.* [10] presented some excellent literature surveys on the subject of diffusive imaging systems. However, imaging systems that are able to time resolve both ballistic and diffusive photons are rather expensive (e.g., a gated optical intensifier camera costs about \$100,000) and are not discussed in this paper. Here, we focus on and derive fundamental performance limits for imaging systems that detect ballistic photons only. We exploit these statistical studies to improve the performance of ballistic imaging systems even in long distances where the signal power is weak.

It is important to note that because of the stochastic nature of photon propagation, I_b , calculated in Eq. (2), is merely the expected value of a Poisson random variable that estimates the number of surviving ballistic photons. Moreover, we assume that the received signal at the detector is contaminated with some amount of independent Poisson noise due to shot noise and other degrading effects. Therefore, since the received signal at the detector is the unweighted summation of two Poisson random variables, it can be modeled as a Poisson random process with the following expected value:

$$I = I_0 \exp(-\mu_t d) + X_e = X_s + X_e,$$

where X_e and X_s are the expected values of the noise and signal, respectively. Note that weighted summation of Poisson random variables in general is not Poissonian, which in some cases can be approximated as a truncated Gaussian distribution [11]. However, summation of Poisson random variables with integer weights is yet another Poisson random variable.

B. Characterizing the Optical Properties of the Medium in the Absence of Targets

Accurate characterization of the scattering medium's optical properties is essential for designing optimal detectors. Since light propagation in ballistic imaging systems is described by the single-parameter Beer's law model, we are mostly interested in measuring (characterizing) the medium or semitransparent object's extinction factor.

In the imaging model of Subsection 2.A, the received signal is modeled as a Poisson random variable with probability density function

$$f(\underline{y} | X_s + X_e) = \prod_{k=1}^N \frac{e^{-(X_{e_k} + X_{s_k})} (X_{e_k} + X_{s_k})^{y_k}}{y_k!}, \quad (3)$$

where y_k is the k th measurement, $\underline{y} = [y_1, y_2, \dots, y_k, \dots, y_N]^T$, $X_e = [X_{e_1}, X_{e_2}, \dots, X_{e_k}, \dots, X_{e_N}]^T$, and $X_s = [X_{s_1}, X_{s_2}, \dots, X_{s_k}, \dots, X_{s_N}]^T$. Note that the laser emits thousands of pulses per second and in practical implementation each spatial position is measured N times to improve the quality of estimation, and therefore the model in Eq. (3) is presented in vector form.

Since the average power of the laser or the detector (and medium) characteristics are assumed not to be changing abruptly, to simplify notations, we assume that $X_{e_1} = X_{e_2} = \dots = X_{e_N} = X_e$ and $X_{s_1} = X_{s_2} = \dots = X_{s_N} = X_s$ (extension to the more general time-varying signal and noise case is straight forward). The maximum likelihood (ML) estimate of the medium's extinction factor is given by

$$\frac{\partial \log[f(\underline{y} | X_s + X_e)]}{\partial \mu_t} = 0 \Rightarrow \hat{\mu}_t = \frac{\ln\left(-\frac{NI_0}{NX_e - \sum_{k=1}^N y_k}\right)}{d}.$$

Study of the Fisher information matrix (FIM) determines the accuracy of the above estimation scheme. Each element of this matrix can be computed [12] as

$$\mathbb{I}_{i,j} = -E \frac{\partial^2 \log[f(\underline{y} | X_s + X_e)]}{\partial \Theta_i \partial \Theta_j} = \sum_{k=1}^N \left(\frac{1}{X_e + X_{s_k}} \frac{\partial X_{s_k}}{\partial \Theta_i} \frac{\partial X_{s_k}}{\partial \Theta_j} \right),$$

where E is the expected value operator and Θ_k is the k th parameter of the model. For the case of characterizing the extinction factor of the medium, the FIM has only one element:

$$\mathbb{I}(\mu_t) = \frac{NI_0^2 d^2 e^{-2\mu_t d}}{X_e + NI_0 e^{-\mu_t d}}.$$

Note that an unbiased estimator can be found that attains the Cramér–Rao bound (CRB), which defines a lower bound on the covariance of any unbiased estimator [13], if and only if the estimator is a linear transformation of the gradient of the log-likelihood (score) function [13,14]

$$\frac{\partial \log[f(\underline{y} | I_0 e^{-\mu_t d} + X_e)]}{\partial \mu_t} \stackrel{?}{=} \mathbb{I}(\mu_t)(\hat{\mu}_t - \mu_t).$$

Now, since

$$\frac{\partial \log[f(\underline{y} | I_0 e^{-\mu_t d} + X_e)]}{\partial \mu_t} = \mathbb{I}(\mu_t) \left[I_0 d e^{-\mu_t d} (X_e + I_0 e^{-\mu_t d}) - \frac{I_0 d e^{-\mu_t d}}{N} \sum_{k=1}^N y_k \right],$$

it is clear that no efficient estimate of the extinction parameter can be found and such estimates will always be biased. This suggests that, in general, the lower bound on the variance of such an estimator cannot be computed by simply inverting the Fisher matrix element. Fortunately, we can numerically show that for the turbid media that are of most interest to us [such as [15] heavy fog ($\mu_t = 12.5^{-1} \text{ m}^{-1}$), light fog ($\mu_t = 125^{-1} \text{ m}^{-1}$), and haze ($\mu_t = 505.05^{-1} \text{ m}^{-1}$)], the bias component relative to the

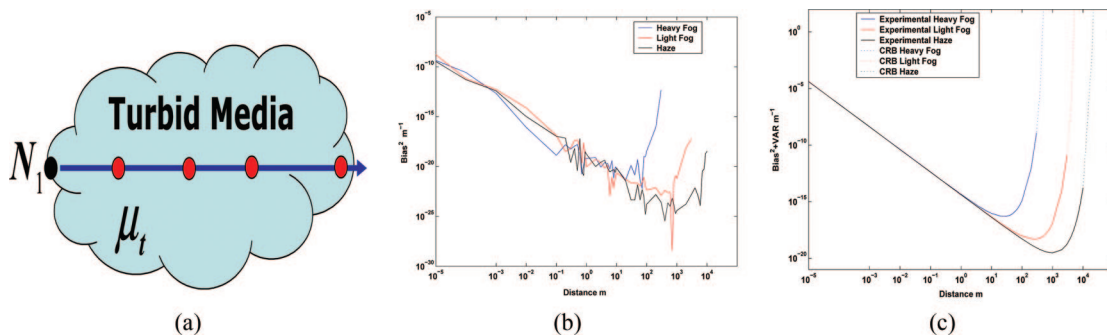


Fig. 1. (Color online) Optimal distance for calibrating the medium extinction factor for heavy fog, light fog, and haze. (a) Experimental setup, where the detector is moved to different locations [marked by lighter (red) dots] inside the turbid medium. (b) Bias of estimation that is calculated over 60,000 Monte Carlo simulations. (c) Summation of squared bias and variance (solid curves) that is dominated by the variance component and perfectly fits the predicted results from CRB formulation (dotted curves) in short distances.

variance is small and can be ignored. Therefore the CRB on the variance can be expressed as

$$\text{Var}(\mu_t) > \frac{X_e + I_0 e^{-\mu_t d}}{N_1 I_0^2 d^2 (e^{-\mu_t d})^2}. \quad (4)$$

Aside from theoretical analysis, in practice, this simple closed-form expression of the lower bound to the variance of the estimate can help us design optimal experiments to characterize the optical properties of the medium and the target.

For example, the CRB analysis helps us find the optimal distance between the laser and the detector for estimating the medium extinction factor. Figure 1(a) shows the setup of this numerical experiment, where the black dot represents the position of the laser and the lighter (red) dots represent the possible locations of the detector. The optimal distance minimizing the lower bound on the estimator variance can be easily calculated by differentiation of Eq. (4) with respect to the distance (d). Figure 1(b) shows the estimated bias for this experiment (via 60,000 Monte Carlo experiments), which are small and negligible. In Fig. 1(c), we have plotted the summation of the numerically experimented bias (squared) and the minimum variance (solid curves) and the CRB (dotted curves) predicted from Eq. (4), which perfectly fit the numerically experimented results in shorter distances. These plots suggest that, for calibrating heavy fog, the optimal distance between the laser and the detector is less than 100 m, whereas such a distance for light fog is of the order of a few hundred meters and for haze is of the order of 1 km. Note that the dotted curves (numerically experimented results) in Figs. 1(b)–1(c) are discontinued after certain distances. The reason for such discontinuity is that in long distances, where the signal power is about the same as the noise level, the estimated bias is not negligible and abruptly tends to infinity. Therefore, the proposed CRB formulation (4), depending on the scattering properties of the medium, is only valid up to some distance as plotted in Fig. 1. Practically, this is of no concern, since these distances are away from the optimal calibration distance.

C. Joint Characterization of the Medium and the Target's Optical Properties

A related and more practical problem, namely, characterizing the optical properties of an object located inside an unknown turbid medium, requires two independent sets of experiments. The first set of experiments is performed in the absence of the object (and repeated N_1 times to improve the accuracy) and the second set of experiments is performed in the presence of the presumed object (and repeated N_2 times). Figure 2 illustrates such an imaging scenario, for which we can easily derive the ML estimates of the medium and the object (inclusion) extinction factors as

$$\hat{\mu}_t = \frac{\ln\left(-\frac{N_1 I_0}{N_1 X_e - \sum_{k=1}^{N_1} y_k}\right)}{d},$$

$$\hat{\mu}_{t_{inc}} = \frac{d \ln\left(-\frac{N_2 I_0}{N_2 X_e - \sum_{k=1}^{N_2} y_k}\right) - (d - d_{inc}) \ln\left(-\frac{N_1 I_0}{N_1 X_e - \sum_{k=1}^{N_1} y_k}\right)}{d d_{inc}},$$

respectively, where d_{inc} is the thickness of the object.

The general FIM formulation of Eq. (4) can be exploited for both of these imaging scenarios. In this

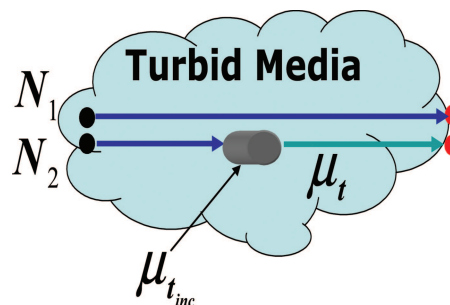


Fig. 2. (Color online) Experimental setup for characterizing the optical properties of the medium (μ_t) and a semitransparent object ($\mu_{t_{inc}}$).

case, the CRBs are derived from the inverse of a $[2 \times 2]$ FIM, the diagonal elements of which define the variance bounds:

$$\begin{aligned}
 \text{Var}(\mu_t) &> \frac{X_e + I_0 e^{-\mu_t d}}{N_1 I_0^2 d^2 (e^{-\mu_t d})^2}, \\
 \text{Var}(\mu_{tinc}) &> \frac{\Omega e^{2\mu_t d - 2\mu_t d_{inc} + 2\mu_{tinc} d_{inc}}}{I_0^2 d^2 N_1 d_{inc}^2 N_2} \\
 \Omega &= (N_1 d^2 X_e + N_1 d^2 e^{-\mu_t d + \mu_t d_{inc} - \mu_{tinc} d_{inc}} I_0 \\
 &\quad + N_2 e^{2\mu_t d_{inc} - 2\mu_{tinc} d_{inc}} d^2 X_e \\
 &\quad + N_2 e^{-\mu_t d + 2\mu_t d_{inc} - 2\mu_{tinc} d_{inc}} d^2 I_0 \\
 &\quad - 2N_2 e^{2\mu_t d_{inc} - 2\mu_{tinc} d_{inc}} d d_{inc} X_e \\
 &\quad - 2N_2 e^{-\mu_t d + 2\mu_t d_{inc} - 2\mu_{tinc} d_{inc}} d d_{inc} I_0 \\
 &\quad + N_2 e^{2\mu_t d_{inc} - 2\mu_{tinc} d_{inc}} d_{inc}^2 X_e \\
 &\quad + N_2 e^{-\mu_t d + 2\mu_t d_{inc} - 2\mu_{tinc} d_{inc}} d_{inc}^2 I_0). \quad (5)
 \end{aligned}$$

As an illustrative example, we fixed N_1 and N_2 to 50 each, $X_e = 20$, and assumed that semitransparent objects with extinction factors of $\mu_{tinc} = 0.124$, $\mu_{tinc} = 1.24$, and $\mu_{tinc} = 12.4$ and 1 m thickness are present inside heavy fog. In Fig. 3, we compared the numerically experimented squared bias and variance (via 5000 Monte Carlo simulations) to the CRB limit, assuming that the distance between the laser and the detector are variant between 50 and 300 m. The results basically show that the numerically experimented and CRB values of the medium extinction factor in all cases are indistinguishably close to each other. On the other hand, as the inclusive object becomes more opaque, the theoretic CRB and numerically experimented variance diverge from each other.

3. Performance Analysis of Pixelwise Optimal Detectors

In this section, assuming that the laser, target, and turbid medium are accurately calibrated, we study the performance bounds of optimal detectors in the presence of opaque or semitransparent objects.

A. Detecting Opaque Objects

In this subsection, we study the performance of the Neyman–Pearson (NP) type statistical test [16] for detecting opaque objects hidden in a turbid medium versus distance. In this test, we basically compare the likelihood of the following two scenarios:

- \mathbb{H}_0 : An opaque object is hidden in the scattering medium, blocking the laser pulse (i.e., measurements contain only noise).
- \mathbb{H}_1 : No opaque object exists in the propagation line of the laser pulse (i.e., measurements contain noise plus an attenuated laser pulse).

The probability density function of these two scenarios when such tests are repeated N times are

given by

$$\begin{aligned}
 \mathbb{H}_0 : f(y|X_e) &= \prod_{k=1}^N \frac{e^{-(X_e)} (X_e)^{y_k}}{y_k!}, \\
 \mathbb{H}_1 : f(y|X_s + X_e) &= \prod_{k=1}^N \frac{e^{-(X_e + X_s)} (X_e + X_s)^{y_k}}{y_k!}, \quad (6)
 \end{aligned}$$

and therefore the NP test is derived by comparing the log-likelihood ratio to a threshold as

$$\log \prod_{k=1}^N \left[\frac{e^{-(X_e + X_s)} (X_e + X_s)^{y_k}}{y_k!} \right] \stackrel{\mathbb{H}_1}{\geq} \gamma \stackrel{\mathbb{H}_0}{\Rightarrow} \sum_{k=1}^N y_k \stackrel{\mathbb{H}_1}{\geq} \frac{\log(\gamma) + NX_s}{\log\left(\frac{X_e + X_s}{X_e}\right)} = \gamma'. \quad (7)$$

Noting that $\sum_{k=1}^N y_k$ is yet another Poisson process, the probabilities of false alarm (P_{FA}) and detection (P_D) are computed as

$$\begin{aligned}
 P_{FA} &= P\left\{ \sum_{k=1}^N y_k > \gamma' \mid \mathbb{H}_0 \right\} = \sum_{k=\gamma'+1}^{\infty} \frac{e^{-NX_e} (NX_e)^k}{k!} \\
 &= 1 - \sum_{k=0}^{\gamma'} \frac{e^{-NX_e} (NX_e)^k}{k!} = 1 - \text{CDF}(NX_e), \quad (8)
 \end{aligned}$$

$$\begin{aligned}
 P_D &= P\left\{ \sum_{k=1}^N y_k > \gamma' \mid \mathbb{H}_1 \right\} = \sum_{k=\gamma'+1}^{\infty} \frac{e^{-NX_e - NX_s} (NX_e + NX_s)^k}{k!} \\
 &= 1 - \sum_{k=0}^{\gamma'} \frac{e^{-NX_e - NX_s} (NX_e + NX_s)^k}{k!} \\
 &= 1 - \text{CDF}(NX_e + NX_s), \quad (9)
 \end{aligned}$$

where CDF is the cumulative distribution function of a Poisson random variable. Note that, in some scientific communities, the false alarm is commonly referred to as a false positive and detection is referred to as a true positive.

Figure 4(a) shows the receiver operating characteristics (ROC) (P_D versus P_{FA}) curves for detecting opaque objects in heavy fog, considering a detector with $X_e = 20$ and a laser power as in Eq. (1). This experiment shows that, by using only ballistic photons, it is possible to reliably detect the existence (or absence) of opaque objects in this scattering medium up to a distance of ~ 30 MFPs. Figure 4(b) shows the system performance curves by fixing the false alarm rate (P_{FA}) at 0.0015, 0.015, and 0.15 values and plotting the detection rate versus distance (P_D versus d).

B. Detecting Semitransparent Objects

Detection of semitransparent objects is based on differentiating between the following two imaging scenarios:

- \mathbb{H}_0 : A semitransparent object is hidden in the scattering medium, partially blocking the laser pulse

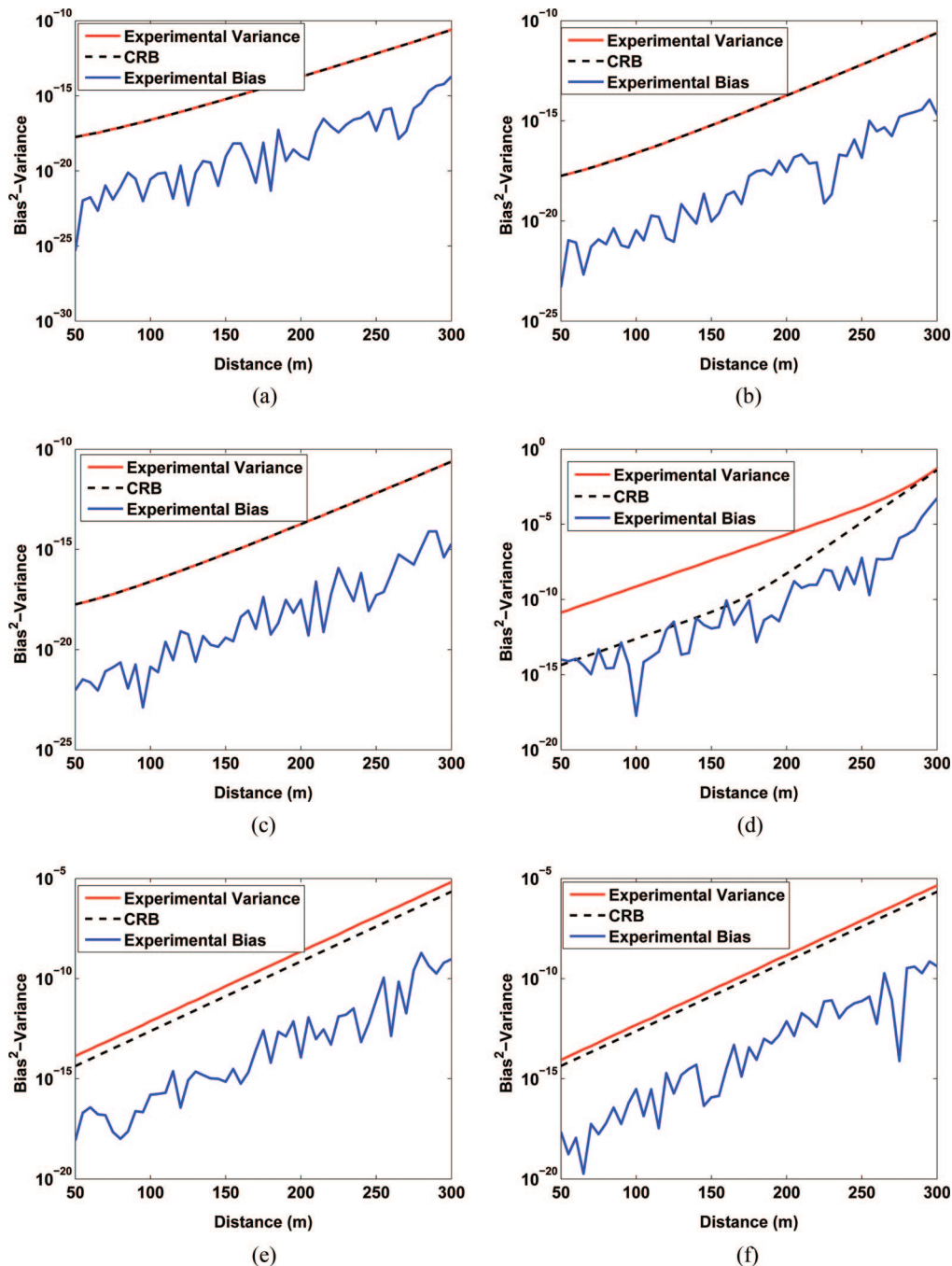


Fig. 3. (Color online) Comparison of the bias and variance from 5000 Monte Carlo simulations (numerically experimented) and the estimated CRB values of the medium and the semitransparent target's optical properties versus distance. The bias, variance, and CRB of the medium extinction factor are compared in (a), (b), and (c). The bias, variance, and CRB of the target's extinction factor are compared in (d), (e), and (f).

(i.e., the measurement is noise plus signal attenuated by both the medium and the target).

- \mathbb{H}_1 : No semitransparent object exists in the propagation line of the laser pulse in the scattering (i.e., measurement is noise plus signal attenuated by the medium).

The number of ballistic photons in the attenuated signal that travel through both the medium and the semitransparent object is calculated as

$$X_{s_{inc}} = I_0 e^{-\mu_{t_{inc}} d_{inc} - \mu_t (d - d_{inc})},$$

where $\mu_{t_{inc}}$ and d_{inc} are the extinction factor and the thickness of the object, respectively. Based on this model, a NP detection rule is derived as

$$\sum_{k=1}^N y_k \underset{\mathbb{H}_0}{\overset{\mathbb{H}_1}{\geq}} \frac{\log(\gamma) + N(X_{s_{inc}} - X_s)}{\log\left(\frac{X_e + X_{s_{inc}}}{X_e + X_s}\right)} = \gamma'. \quad (10)$$

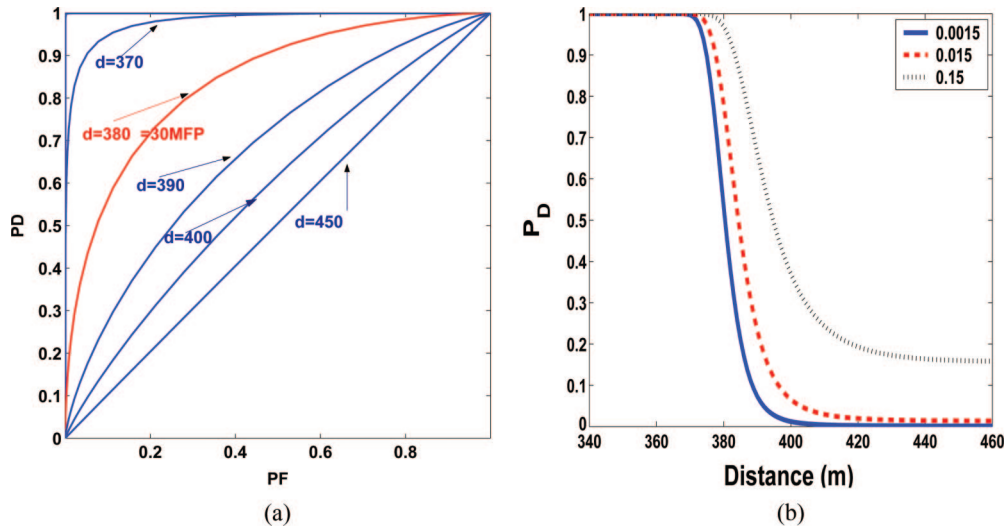


Fig. 4. (Color online) (a) ROC plots at different distances for detecting opaque objects in heavy fog ($\mu_t = 12.5^{-1} \text{ m}^{-1}$) and $X_e = 20$. (b) By fixing the P_{FA} at different values, the detection rate (P_D) is plotted versus the distance.

The probabilities of false alarm and detection are computed as

$$\begin{aligned}
 P_{FA} &= P\left\{\sum_{k=1}^N y_k > \gamma' \mid \mathbb{H}_0\right\} = \sum_{k=\gamma'+1}^{\infty} \frac{e^{-NX_e - NX_s} (NX_e + NX_s)^k}{k!} \\
 &= 1 - \sum_{k=0}^{\gamma'} \frac{e^{-NX_e - NX_s} (NX_e + NX_s)^k}{k!} \\
 &= 1 - \text{CDF}(NX_e + NX_s), \tag{11}
 \end{aligned}$$

$$\begin{aligned}
 P_D &= P\left\{\sum_{k=1}^N y_k > \gamma' \mid \mathbb{H}_1\right\} = \sum_{k=\gamma'+1}^{\infty} \frac{e^{-NX_e - NX_{s_{inc}}} (NX_e + NX_{s_{inc}})^k}{k!} \\
 &= 1 - \sum_{k=0}^{\gamma'} \frac{e^{-NX_e - NX_{s_{inc}}} (NX_e + NX_{s_{inc}})^k}{k!} \\
 &= 1 - \text{CDF}(NX_e + NX_{s_{inc}}). \tag{12}
 \end{aligned}$$

Figure 5 shows the ROC curves for detecting a semitransparent object in heavy fog. In this experiment using a laser and detector similar to the ones in Subsection 3.A, the distance was fixed at 300 m, which according to Fig. 4 delivers almost perfect detection for opaque objects. Figure 5(b) shows the system performance curves by fixing the false alarm rate (P_{FA}) at 0.00015, 0.0015, and 0.015 values and plotting the detection rate versus the object's extinction factor (P_D versus $\mu_{t_{inc}}$). As expected, this experiment shows that the detection performance deteriorates as the object becomes less opaque.

C. Multipixel GLRT Detection

As explained in Subsection 2.A, in ballistic imaging the field of view is scanned at multiple points to create a 2-D image of the objects in the ROI. In this subsection, we propose an effective algorithm that

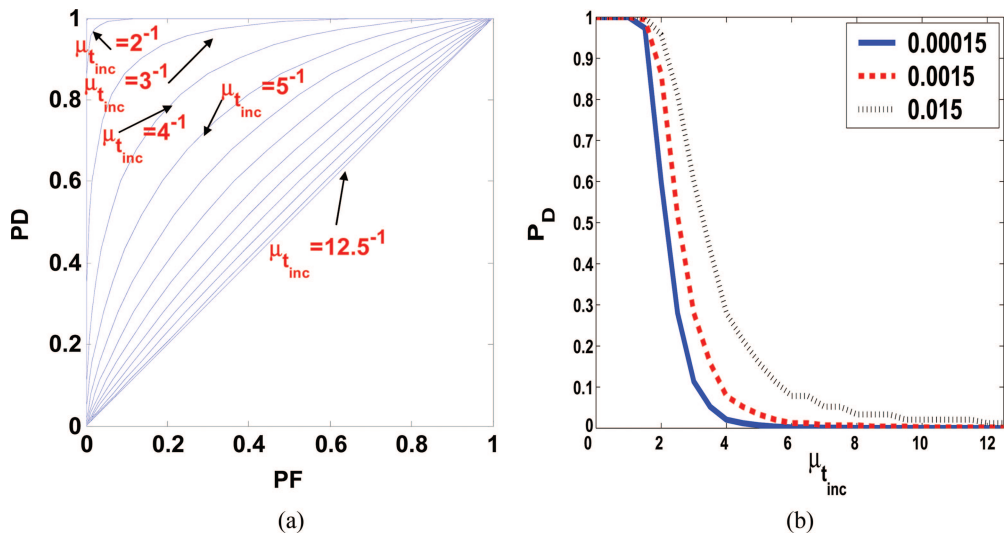


Fig. 5. (Color online) (a) ROC plots for detecting transilluminative objects at 300 m distance in heavy fog ($\mu_t = 12.5^{-1} \text{ m}^{-1}$) and $X_e = 20$. (b) By fixing the P_{FA} at different values, detection rate (P_D) is plotted versus the object's transparency ($\mu_{t_{inc}}$).

exploits the spatial correlation of the nearby samples in a multipixel imaging scenario to improve on the performance of the single-pixel optimal detectors developed in the previous section.

The proposed multipixel detection technique generalizes the single-pixel detection techniques and performs tests on superpixels, which are the collective intensities of a set of neighboring pixels in size and shape of the hidden objects. However, since in general the size and shape of the hidden objects is not known *a priori*, we develop a GLRT-based algorithm that simultaneously tests the existence and also estimates the shape and size of the objects hidden in turbid media.

The outline of the proposed GLRT algorithm is illustrated by an example in Fig. 6. First, for a given (fixed) false alarm rate the optimal detectors developed in the previous section are exploited to test the existence or absence of objects at each individual pixel. As an illustrative example, this test is applied to the central pixel (shaded) of Fig. 6(a), where the measured pixel value (0.4) is compared with the NP

test threshold (0.5). Of course, the greater the distance of the measurement from the threshold, the more confident we are in the accuracy of the test result. Next, we integrate the gray-level values of all immediate neighboring pixels, and in effect consider them as one superpixel, as illustrated in Fig. 6(b). Since the false alarm rate is fixed for all scales, the decision threshold is different than the threshold calculated in the previous step, which is recalculated based on the gray-level value of the superpixel. In the next steps, we repeat this process by fixing the false alarm rate and considering larger neighborhoods. The generalized NP test for these steps is formulated as follows:

$$y_{m,l}^{scale} \underset{H_0}{\overset{H_1}{\geq}} \frac{\log(\gamma^{scale}) + N_{scale} X_s}{\log\left(\frac{X_e + X_s}{X_e}\right)}, \quad (13)$$

where $y_{m,l}^{scale}$ is the summation of the pixel values in the $N_{scale} = N(2 \times scale - 1)^2$ pixels neighborhood around the pixel at position $[m, l]$. Our confidence in the decision made on each scale is simply defined as the distance between the summation of measurements in the superpixel and that of the threshold set by the GLRT:

$$\text{Confidence}_{m,l}^{scale} = \left| y_{m,l}^{scale} - \frac{\log(\gamma^{scale}) + N_{scale} X_s}{\log\left(\frac{X_e + X_s}{X_e}\right)} \right|. \quad (14)$$

Finally, we decide on the presence or absence of the object at a particular pixel based on the test result of the scale that shows the highest confidence value. Note that the optimal scale is not unique for all pixels, as finer scales are more suitable for pixels located on the texture or edge areas, and coarser scales are more suitable for the pixels located in flat areas. The memory requirements of this technique are independent of the maximum scale number, since we only need to keep the original image, the last estimated image, and the corresponding confidence values.

To have a better understanding of the proposed multiscale GLRT technique and its performance, we set up an illustrative controlled imaging scenario. Figure 7(a) shows an ideal (noiseless and deterministic) image of objects of different sizes and shapes. To depict an experiment at the limit distance where the signal of interest is weak, we consider an imaging scenario in which the average number of received ballistic photons for each pixel is one photon. Figure 7(b) shows such Poisson random signals (free of additive noise effect).

Detection of such signals becomes more difficult when we consider the system noise as illustrated in Figs. 8(a) and 9(a), where the Poisson noise variances (mean) are 20 and 40, respectively. Figs. 8(b) and 9(b) are images reconstructed by implementing the point-

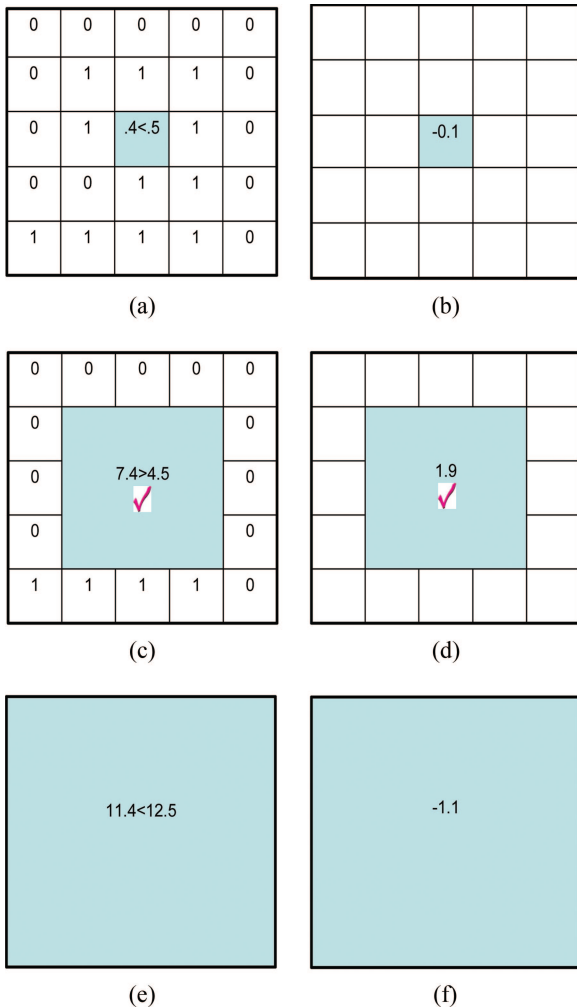


Fig. 6. (Color online) Illustrative example showing the outline of the proposed multiscale GLRT algorithm. The check-marked second scale gives the highest confidence value for the central pixel.

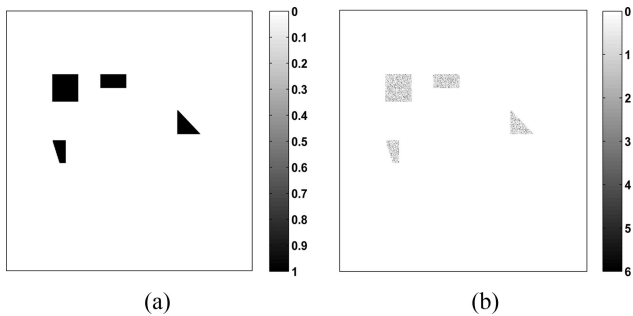


Fig. 7. (a) Ideal deterministic and noise-free image of four objects of different sizes and shapes. (b) Corresponding image as a Poissonian noise-free stochastic signal, with $X_s = 1$.

by-point single-pixel detection techniques, considering a false alarm rate of 0.00125, where none of the objects are correctly identified. On the other hand, Figs. 8(c) and 9(c) are the results of exploiting the multiscale GLRT techniques, showing a considerably more accurate detection of such objects. Figures 8(d) and 9(d) illustrate the scale from which each pixel in the final images of Figs. 8(c) and 9(c), respectively, are selected. Note that, as expected, the pixels in the flat area are selected from the coarser scales, whereas the pixels on the edge areas are selected from the finer scales. Figures 8(e) and 9(e), show the confidence in the detection result (14) with respect to the corresponding pixels. These figures show higher confidence levels in the flat and less confidence in the

edge areas. Also, in Fig. 9(e) we see that the area with the lowest confidence is the place where most misclassifications happen. This is good news, since to increase the detection rate, we may opt to do a second (and faster) round of scans, sampling only on these very low-confidence regions. In Figs. 8(f) and 9(f), we plot the misclassification rates at each scale (curve), and compare it with the overall multiscale rate (line). These numerically experimented plots show that the performance of the proposed pixelwise GLRT technique (depending on the noise level) is either very close to [Fig. 8(f)] or even better than [Fig. 9(f)] the best fixed-scale technique. In Figs. 10(a) and 10(b), the performance of the single-pixel detection technique is compared with the multiscale ones via their corresponding ROC curves. Once again, the multiscale technique shows the best or close to the best performance.

4. Diffraction Effects

So far in this paper, all detection tests and related performance analysis were derived based on a simplified model of light propagation that ignores diffraction. Although such approximation works well for many practical applications, it is not a suitable model for detecting or imaging relatively small sized objects. In this section, we present statistical analysis of the resolution limits in ballistic imaging systems by defining the smallest size of resolvable objects in a turbid medium at given false alarm and detection rates.

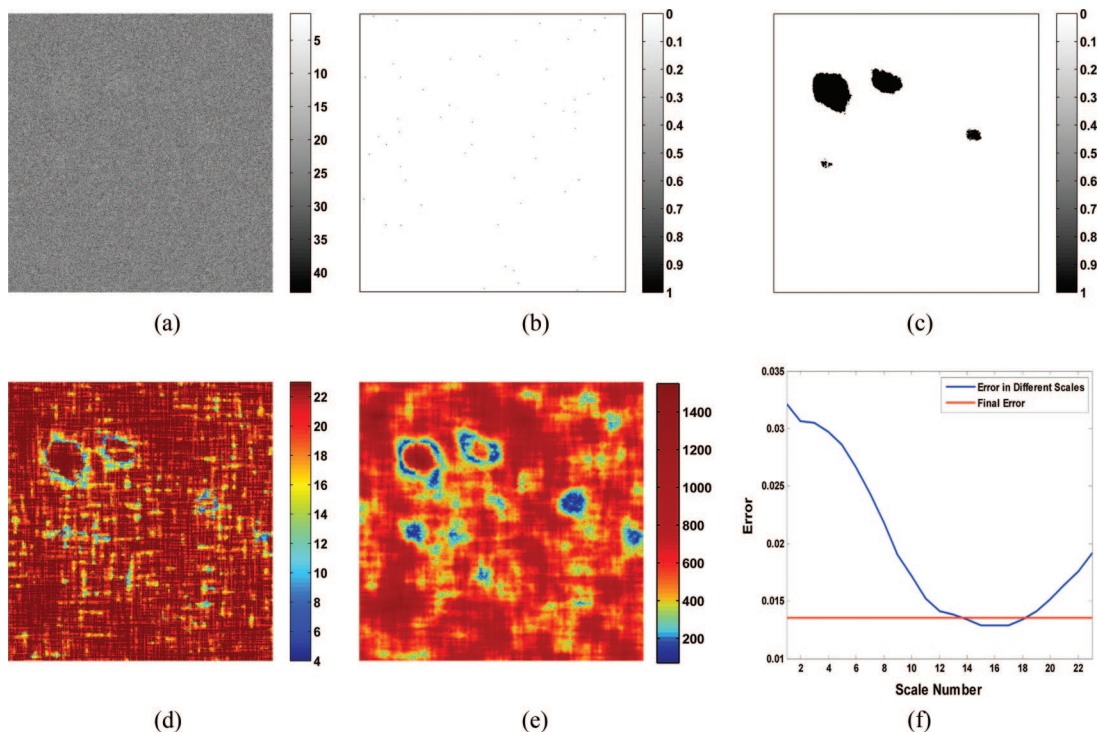


Fig. 8. (Color online) Application of the proposed multiscale GLRT technique for improving the detection rate. (a) Result of adding Poisson noise ($X_c = 20$) to Fig. 7(a). (b) Result of the single-pixel detection. (c) Result of the proposed multiscale detection technique. (d) Image that corresponds to the selected scales for the image shown in (c). (e) Corresponding confidence values. (f) Misclassification probability in different scales.

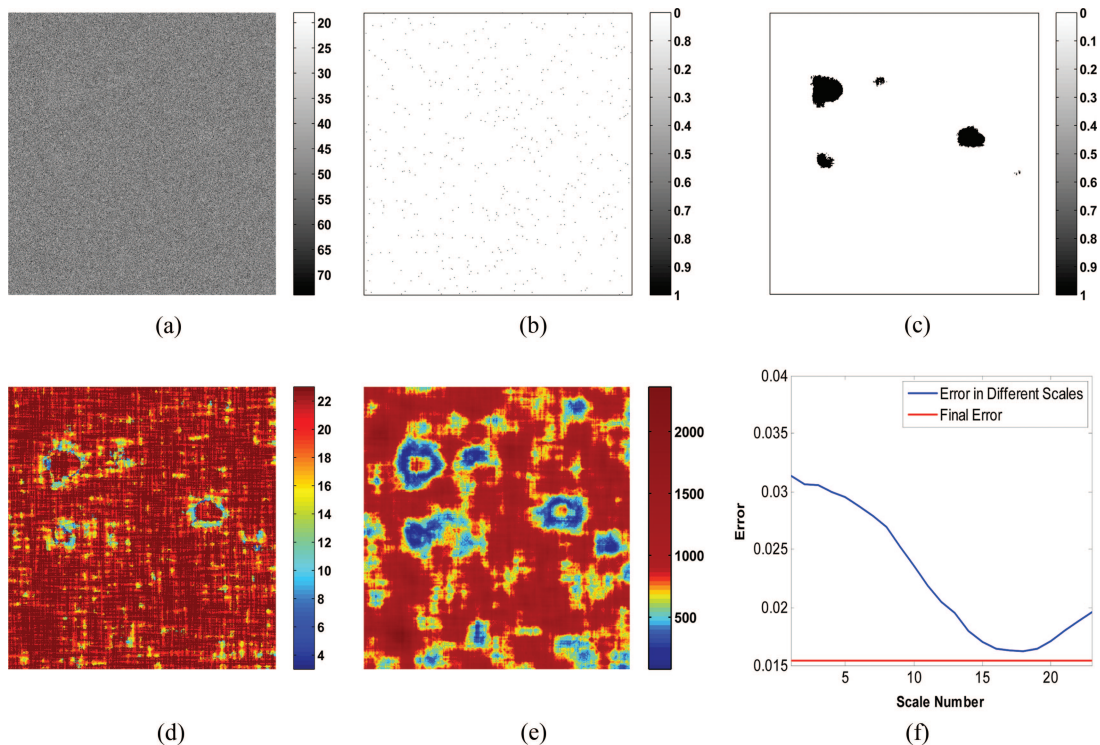


Fig. 9. (Color online) Application of the proposed multiscale GLRT technique for improving the detection rate. (a) Result of adding Poisson noise ($X_e = 40$) to Fig. 7(a). (b) Result of the single-pixel detection. (c) Result of the proposed multiscale detection technique. (d) Image that corresponds to the selected scales for the image shown in (c). (e) Corresponding confidence values. (f) Misclassification probability in different scales.

Our study is the continuation of previous work [17], generalized by considering the effects of the turbid medium and ballistic imaging setup.

Figure 11 is a 1-D illustration of the diffraction, which is described as “any deviation of light rays from rectilinear paths which can not be interpreted as reflection or refraction” [18]. In this figure, the dashed (red) line represents the case in which light propagates in a straight line creating a sharp-edged

shadow of a hidden opaque object at the detector. The solid (green) curve, on the other hand, illustrates a more realistic case in which the object’s shadow appears blurry at the detector as a result of diffraction.

The blur induced by diffraction can be calculated from the Helmholtz–Kirchhoff wave propagation equations [19]. However, for the experimental setups that are of most interest to us with respect to the scope of this paper, the diffraction effect can be taken

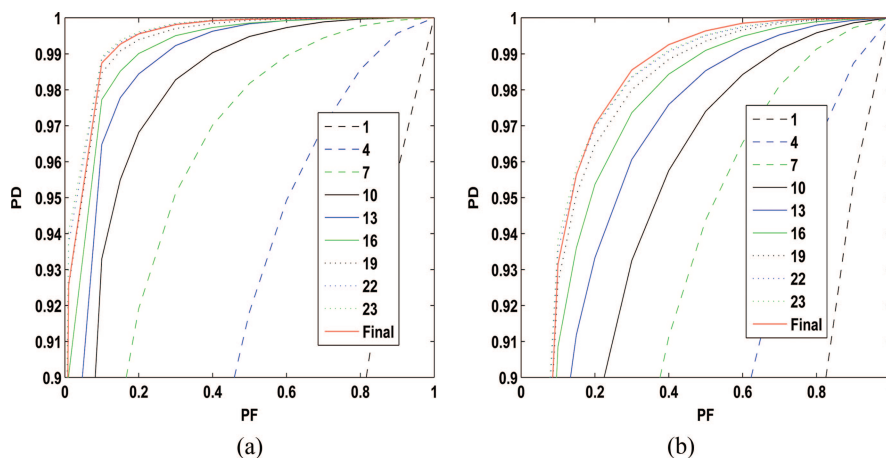


Fig. 10. (Color online) Application of the proposed multiscale GLRT technique for enhancing the detection rate. ROC plots for the proposed multiscale detection scenario in the imaging scenarios of Figs. 8 and 9 (with 25 Monte Carlo experiments) are shown in (a) and (b), respectively. The numerical labels “1, 4, . . . , 23” correspond to the scale at which detection tests are performed, and the plot labeled “Final” represents the performance of the proposed multiscale (fused) technique.

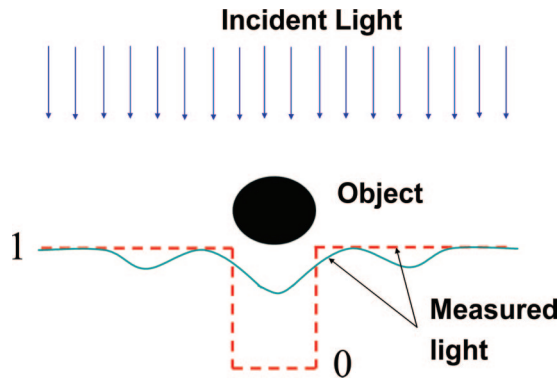


Fig. 11. (Color online) Shadow of an opaque object illuminated by a homogeneous widespread light beam. The dashed (red) curve represents the intensity of the measured light ignoring diffraction. The solid (green) curve represents the diffraction-induced PSF.

into account by convolving the expected signal value with an appropriate point-spread function (PSF) that describes the blurring effect of an object estimated from the Fraunhofer approximation. For a circular opaque object, such a PSF is given by

$$H(r) = 1 - \frac{2k\rho^2}{z} \sin \frac{kr^2}{2z} \frac{J_1\left(\frac{k\rho r}{z}\right)}{\frac{k\rho r}{z}} + \frac{k^2\rho^4}{z^2} \left[\frac{J_1\left(\frac{k\rho r}{z}\right)}{\frac{k\rho r}{z}} \right]^2, \quad (15)$$

where $k = 2\pi/\lambda$ is the wavenumber, $J_1(\cdot)$ is the order 1 Bessel function of the first kind, ρ is the radius of the opaque object, r is the radius coordinate in the detector plane, and z is the distance between the object and the detector [20]. Note that the Fraunhofer approximation is only valid when $z \gg 4\rho^2/\lambda$, and therefore in this paper we only consider far-field imaging scenarios. Ignoring the effect of a turbid medium and considering homogeneous illumination with intensity I' at the object plane, the radially sym-

metric intensity of the detected signal at the radius coordinate r is simply given by $I = I'H(r)$. Figure 12(a) shows the diffraction pattern of a circular opaque object with a distance of $z = 100$ m from the detector, illuminated by unit-intensity ($I' = 1$) light with 800 nm wavelength.

In the imaging scenarios considered in this paper, the detected signal is further attenuated by the turbid medium, and the expected value of the signal intensity at the radius coordinate r and distance z from the object plane can be approximated as

$$I = I' \exp(-\mu_r z) H(r),$$

where we have ignored the fact that due to diffraction some parts of the wavefront travel slightly longer distances. Note that in practice, due to the far-field imaging assumption, such variance in attenuation is small. This effect is shown in Fig. 12(b), where the path lengths L_1 and L_2 are practically equal if the distance between the opaque object and the detector (z) is significantly larger than the PSF spread. The detection problem associated with the signal model defined above is described in the following two imaging scenarios:

- \mathbb{H}_0 : An opaque object of unknown but small size ($\rho > 0$) is hidden in the scattering medium, blocking and blurring the laser pulse (i.e., measurements contain noise plus attenuated and blurred laser pulse).
- \mathbb{H}_1 : No opaque object exists ($\rho = 0$) in the propagation line of the laser pulse (i.e., measurements contain noise plus attenuated laser pulse).

The above GLRT detector is different than the NP detectors of Section 3 since the size of the object is now assumed to be unknown. Following Eq. (2), the expected value of the intensity in the absence of the object (\mathbb{H}_1) is given by

$$I(k, 0) = I_0 e^{-\mu_r d} + X_e.$$

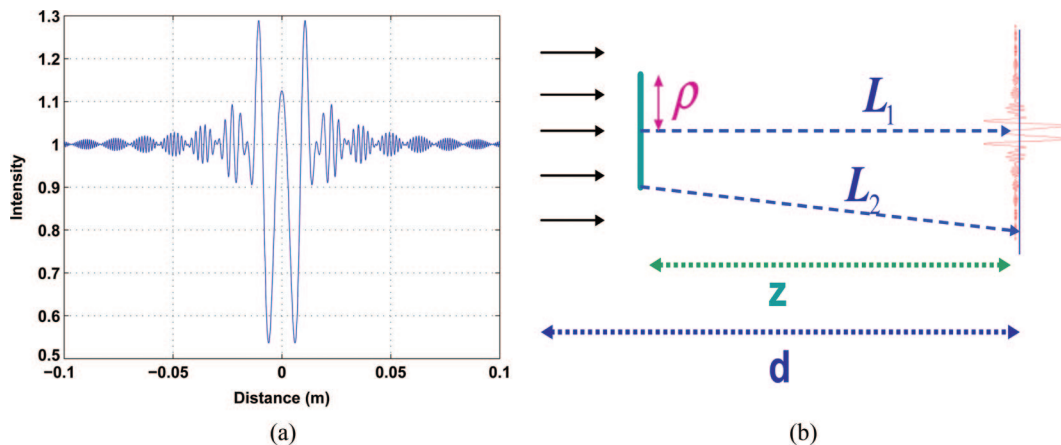


Fig. 12. (Color online) (a) 1-D slice of the diffraction pattern of a circular object of radius 3 mm at 100 m distance and 800 nm wavelength. (b) 1-D slice of the imaging scenario, where z is the distance between the opaque circular object (radius ρ) and the detector. d is the distance between the laser and the detector. The pass length $L_1 \approx L_2$ when z is very long.

The intensity of the signal in the presence of the object (H_0) is estimated as

$$I(k, \hat{\rho}) = I_0 e^{-\mu_t d} H(r_k) + X_e, \quad (16)$$

where $\hat{\rho}$ is the estimate of the opaque object's radius and r_k is the radial distance of the k th pixel from the axes passing through the center of the object. The unknown radius of the opaque object is estimated as

$$\hat{\rho} = \arg \max_{\rho} \prod_{k=1}^N \frac{e^{-I(k, \rho)} [I(k, \rho)]^{y_k}}{y_k!}. \quad (17)$$

The above ML estimate of the radius is solved by numerical optimization, where we discretize ρ over an assumed range of values $\rho[g]$, $g = 1, \dots, G$, and compute the cost function,

$$\varrho[g] = \sum_{k=1}^N y_k \log\{I(k, \rho[g])\} - I(k, \rho[g]). \quad (18)$$

The value of g for which $\varrho[g]$ takes on the largest value is g_{max} , and finally the GLRT detection statistics is given by

$$\sum_{k=1}^N y_k \log\left\{\frac{I(k, \rho[g_{max}])}{I(k, 0)}\right\} \geq \gamma. \quad (19)$$

As an illustrative example, by fixing the false alarm rate at $P_{FA} = 0.1$, the noise level at $X_e = 20$, and assuming a large detector that detects all the light, regardless of the distance or size of the object, we used the above GLRT framework to search for the smallest detectable object size at different distances and detection rates in heavy fog ($\mu_t = 12.5^{-1} \text{ m}^{-1}$). Figure 13 illustrates the result of this experiment, where as expected the size of detectable objects first rises as the distance increases.

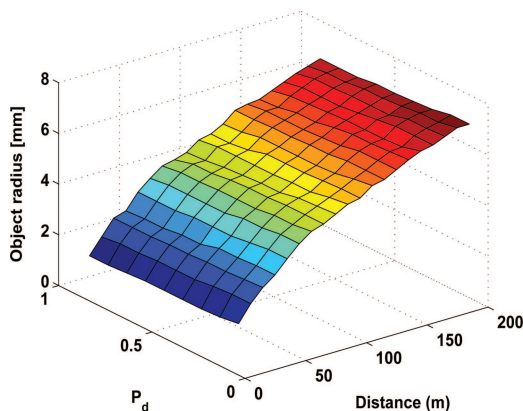


Fig. 13. (Color online) Detection rate versus the (unknown) opaque circular target's radius and the distance between the laser and the detector considering the diffraction limit with $P_{FA} = 0.1$ and $X_e = 20$ in heavy fog ($\mu_t = 12.5^{-1} \text{ m}^{-1}$).

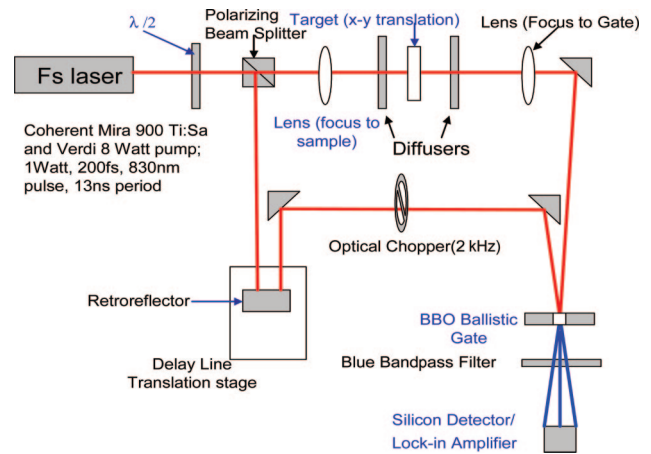


Fig. 14. (Color online) Laser setup at the Ballistic Imaging Laboratory at the University of California, Santa Cruz.

5. Laboratory Setup and Experiments

A. Conventional Ballistic Imaging Experimentation

In our experiments, to generate ultrashort optical pulses we used a Coherent Mira 900 Ti:sapphire tunable femtosecond laser pumped by an 8 W pump (Verdi V-8). At the output this laser generates an average power of ~ 1 W with pulses of 200 fs duration, 13 ns repetition period, and 830 nm wavelength.

As shown in Fig. 14, each laser pulse passes through a $\lambda/2$ plate and is incident on a polarizing beam splitter that divides the pulse into two copies, one used for triggering the ultrafast time gate while the other passes through the scattering medium (which is modeled by two sets of solid diffusers located in front and back of the target). Rotation of the $\lambda/2$ plate determines the power ratio between the two pulses, and we experimentally determined that the best results are achieved in a near 50%/50% splitting ratio. After passing through the diffusers and target, the ballistic photons are incident on the gate at exactly the same time as the triggering pulse and pass through the ultrafast time gate, where due to the phase and polarization difference the scattered photons are rejected. In practice, the triggering pulse timing is controlled by a delay line, which increases or decreases the optical path length, using a computer-controlled translation stage.

The ultrafast time gate used is a nonlinear crystal, β -barium borate (BBO) [21], which utilizes a two-photon process such that the gating time can be as short as the laser pulse width. Additionally, by slightly changing the incident angles of the two pulses on the nonlinear crystal, the time-gated result can be spatially separated from the background signal, greatly increasing the signal-to-noise ratio. This effect is sometimes referred to as background-free cross correlation [22]. The energy of the ballistic photons are then measured by a silicon detector and a lock-in amplifier. The entire setup implemented at the ultrafast imaging laboratory at the University of

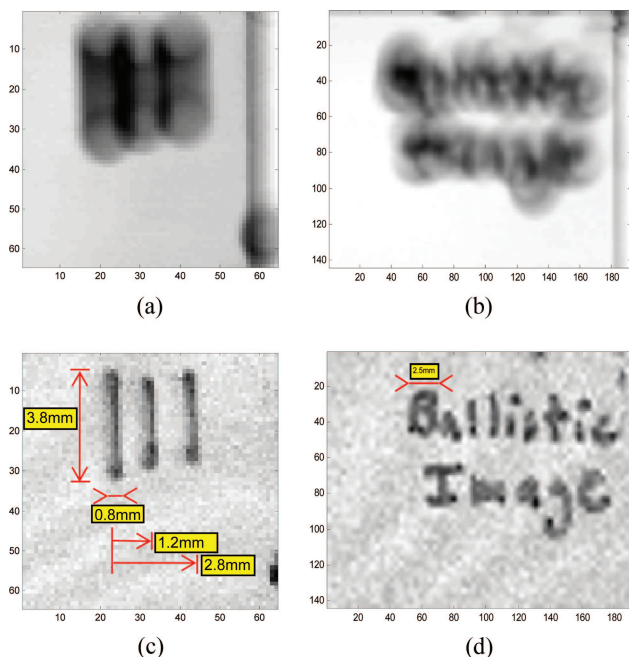


Fig. 15. (Color online) Comparison of diffusive and ballistic imaging. (a), (b) Two diffusive (no time gating) scans. (c), (d) Two corresponding ballistic (time-gated) scans through five solid ground glass diffusers.

California, Santa Cruz, is controlled using LabView and a general purpose interface bus (GPIB) bus.

Figure 15 shows the results of two imaging experiments where the objective is to read the text written on transparency sheets by a ballpoint pen, surrounded by a total of five solid glass (Thorlabs ground glass, DG10-220) diffusers. The thickness of these diffusers is 2 mm each, with the MFP of 0.73 mm (7.3 MFP total). We also note that the dynamic range of our system is approximately 100 dB. Figures 15(a) and 15(b) show the result of scans in the absence and Figs. 15(c) and 15(d) show the result of scans in the presence of the ballistic time gate, without any post-processing. To acquire the nongated images, the gate was removed and the detector repositioned. Note that Figs. 15(a) and 15(c) illustrate raw data (without any postprocessing) from the imaging system, whereas the results shown in Figs. 15(b) and 15(d) are each upsampled by a factor of 3 via the bicubic interpolation technique. These results show that, although ballistic images are noisier than the non-time-gated (diffusive) ones, they are preferable since they are virtually blur free.

B. Adaptive Sampling Experimentation

As explained in the previous sections, in ballistic imaging, 2-D images of the objects in the scattering media are created by a relatively time-consuming point-by-point scanning scheme in which the field of view (FOV) is sampled at regularly spaced locations. For instance, in a typical laboratory setup with a mechanical translation stage (Fig. 14), creating a 256×256 image (i.e., sampling at 65,536 points)

takes about 4 h, which might be prohibitively long for many real-world applications. Although such excessive time can be reduced if the mechanical translation stage is replaced by a more expensive optical one, faster scans are always desired, and moreover, for many applications, the total number of pulses delivered in a given time period is limited by the average delivered energy due to health concerns.

By making some simplifying assumptions about the objects of interest (e.g., piecewise constancy), irregular scan strategies, such as sampling sparsely in the low-frequency areas and densely in the high-frequency (edge or textured) areas, are shown to be useful in reducing the imaging time. Recently, two related techniques, namely, compressive sensing [23,24] and active learning [25] (adaptive sampling) were proposed to reduce the number of samples required to achieve certain reconstruction accuracy with respect to the regular (passive) scanning technique. We note that it is the sparsity of the signal of interest (in a given overcomplete dictionary of bases) that enables such techniques to gather sufficient information to achieve optimal (if not perfect) reconstruction in the presence of noise, even when the sampling rate is lower than the Nyquist rate [26]. In the compressive sensing technique, random projections of the signal of interest onto an overcomplete set of basis functions are sequentially recorded. Such random projections in practical optical imaging scenarios can be implemented by passing a wide-field beam through binary masks with a random pattern [in practice, a digital micromirror device can be used to generate the random basis patterns [27]]. Unfortunately, in the ballistic imaging setup, creating a wide-field beam is not easy. Moreover, diffraction limits the resolution of the binary mask and therefore implementing a compressive-sensing-based ballistic imaging system is not trivial. On the other hand, in the following we show that adaptive sampling techniques can be readily exploited for ballistic imaging purposes.

We have implemented adaptive sampling as a two-step process [28]. In the first step, we regularly sample the FOV space at $N/2$ points, where N is the total number of samples that we plan to collect. We use these $N/2$ measurements to create a pilot estimate of the unknown FOV. In the next step, the remainder of the $N/2$ points are used to sample the FOV on the edge areas of the estimated image. It can be shown that the decay rate of the mean square error for piecewise constant images is $O(N^{-1/2})$ and $O(N^{-1})$ for the passive and active sampling techniques, respectively [28].

We also note that active learning relies on accurate adaptive image reconstruction algorithms to reconstruct the unknown images from the irregular samples of the FOV. In our implementation, we used an image reconstruction method based on maximum *a posteriori* (MAP) with bilateral total variation prior (regularizer) [29]. The general formulation of this

technique is presented as follows:

$$\hat{X}(t) = \arg \min_{X(t)} \left[\|A(X - \hat{Z})\|_2^2 + \psi \sum_{l,m=-P}^P \alpha^{|m|+|l|} \|S_x^l S_y^m X\|_1 \right], \quad (20)$$

where X of size $[ML \times 1]$ is a vector representing the reconstructed image of size $[M \times L]$ after lexicographic ordering, and Z of size $[ML \times 1]$ is a vector that stores the $N < ML$ measurements. In this vector, the elements that correspond to those pixels in X for which no measurement is available are filled with zeros. The matrices S_x^l and S_y^m are the operators corresponding to shifting the image represented by X by l pixels in the horizontal direction and m pixels in the vertical direction, respectively. The scalar weight, $0 < \alpha \leq 1$, is applied to give a spatially decaying effect to the summation of the regularization terms, which in effect represent derivatives across multiple resolution scales. Matrix A of size $[ML \times ML]$ is a diagonal matrix whose values are chosen in relation to our confidence in the measurements that contributed to make each element of \hat{Z} (diagonal elements corresponding to pixels for which no measurement is available are replaced with zeros). The regularization

parameter, ψ , is a scalar for properly weighting the first term (data fidelity cost) against the second term (regularization cost).

To validate the applicability of this adaptive sampling and reconstruction technique versus the common passive sampling technique, we performed the following experiment. A metal washer was imaged through a ground glass diffuser (Thorlabs ground glass, DG10-220) via the ballistic imaging setup of Fig. 14. Figure 16(a) shows the result of scanning the medium on a 128×128 (16,384 total) regularly sampled grid. Figure 16(b) shows the same image sampled on a regular 32×32 (1024) grid and then upsampled by the bicubic interpolation method to a dense 256×256 grid. The alternative sampling strategy was performed by exploiting the same experimental setup (distance, turbid medium, target), where a total of 950 irregularly sampled data points were collected in the said two-step adaptive process. Figure 16(c) shows the result of such an adaptive sampling scheme after upsampling to the 256×256 grid by the proposed adaptive MAP-based interpolation method. The spatial position of the 984 adaptive samples are marked as white dots on a 256×256 grid in Fig. 16(d), which, as expected, is considerably denser on the edge areas.

6. Conclusion and Future Work

In this paper, we have studied a technique for capturing high-resolution images through turbid media. This approach was based on separating the unscattered (ballistic) photons from the diffused ones by implementing an ultrafast time-gating system. The novelty of this paper is in combining the recent advances in optical science with the novel image processing and statistical signal processing techniques. We studied the resolution limits of such a system that were close to diffraction (Rayleigh) limits for longer distances. We derived the fundamental limits on the accuracy of the estimated extinction parameters of an unknown turbid medium and the targets inside it. This study also guided us toward the most efficient experiments (with respect to both time and accuracy) for calibrating the model parameters of the unknown turbid medium as well as the optical properties of the target (which can be used to identify and categorize it). Our results showed that for a medium of practical interest, namely, heavy fog, optical parameters can be estimated with high accuracy. We used the said model to derive optimal statistical tests for detecting objects hidden in turbid media. Performance analysis was carried out by computing ROC curves for the proposed optimal tests, showing that, by considering only the ballistic photons, we are able to detect opaque objects hidden in heavy fog in the range of approximately 380 m (i.e., 30 MFPs). The detection rate of the semitransparent objects is shown to be slightly less than this distance. Also, real experiments attested to the fact that ballistic imaging, especially in longer distances, is difficult, and therefore we developed a multiscale GLRT algorithm to improve the detection rate in such scenarios. To reduce

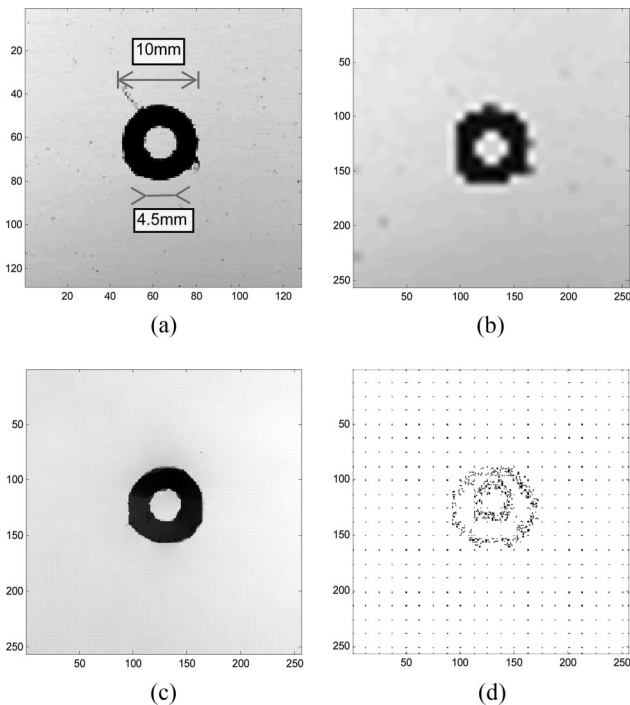


Fig. 16. Comparison of passive and active imaging. (a) Result of scanning the turbid medium on a regular 128×128 grid (16,384 dense passive sampling). (b) Result of scanning the turbid medium on a regular 32×32 grid (1024 sparse passive sampling) followed by interpolation via bicubic interpolation to reconstruct the image on a 256×256 grid. (c) Result of scanning the turbid medium on an irregular grid (984 sparse adaptive sampling) followed by interpolation via adaptive interpolation to reconstruct the image on a 256×256 grid. (d) Distribution of the 984 irregular samples.

the data acquisition time that is essential for many real-world applications, we implemented an adaptive sampling scheme that significantly reduced the data acquisition time.

As for future work, one may exploit temporal, spatial, and wavelength diversity and coding for ballistic imaging. We can study the array imaging framework where multiple emitters will transmit coordinated pulses of light, and for their part, a collection of photon-detecting elements will gather the received data and compute a resultant image. Furthermore, there is the possibility of analyzing various ways of coding these pulses (e.g., transmitting sequences of pulses as is done in ultrawideband communications).

Moreover, we believe that detection techniques that exploit all ballistic, snake, and diffused photons [30] (what we term holistic imaging and detection) enable detection of larger objects at significantly longer range. More theoretical and experimental work needs to be done to design a (near) optimal yet practical solution to this important problem.

Appendix A: Decision-Theoretic Resolution Bounds

As explained throughout this paper, the diffraction-limited resolution of ballistic imaging systems [e.g., Figs. 15(c) and (d)] makes them appealing for imaging in relatively short distances. However, in relatively long distances the ballistic signal is too weak and we are bound to rely on the blurry but higher signal-to-noise ratio (SNR) images of conventional imaging systems [e.g., Figs. 15(a) and (b)]. In this Appendix, we adapt a decision-theoretic approach to the resolution bounds and search for the critical distance after which the ballistic imaging systems are of no practical advantage compared with the conventional imaging systems.

1. Ballistic Imaging—Single Point

The problem of determining whether an object lies along the line of sight can be cast as a statistical hypothesis test as follows. Given a received photon count X at the sensor, one must choose between two possible situations. The first situation is that no occluding object exists in the path between the laser and the sensor (\mathbb{H}_0). The alternative is that there is an occluding object along the line of sight between the laser and the detector (\mathbb{H}_1). Semitransparent objects can be considered to be significantly more scattering than the medium [31], and therefore the detector will collect an attenuated number of ballistic photons (compared with \mathbb{H}_0) along with the noise photons.

Following the notation of Subsection 3.B, we define the number of noise photons that will arrive at the detector as $\mathcal{P}(NX_e)$, where $X \sim \mathcal{P}(\chi)$ is a Poisson-distributed random variable with mean χ . Then, the hypothesis test is given by the null hypothesis defined as $\mathbb{H}_0 : X \sim \mathcal{P}(NX_e + NX_s)$ and the alternate hypothesis (object exists) defined as $\mathbb{H}_1 : X \sim \mathcal{P}(NX_e + NX_{s_{inc}})$. As the mean of the Poisson distribution grows, the probability distribution tends to a Gaussian, e.g., averaging many repeated Poissonian trials (i.e., N large) results in a Gaussian-distributed sta-

tistic. Using the Anscombe transformation [31], we obtain the following relationship:

$$X \sim \mathcal{P}(\chi) \Rightarrow 2\sqrt{X + \frac{3}{8}} \sim \mathcal{N}(2\sqrt{\chi}, 1),$$

where $\mathcal{N}(\zeta, \sigma^2)$ represents Gaussian distribution with mean ζ and variance σ^2 . Defining a new variable representing the Anscombe-transformed statistic $X' = 2\sqrt{X} + 3/8$ the hypothesis test becomes

$$\mathbb{H}_0 : X' \sim \mathcal{N}(2\sqrt{NX_e + NX_s}, 1),$$

$$\mathbb{H}_1 : X' \sim \mathcal{N}(2\sqrt{NX_e + NX_{s_{inc}}}, 1). \quad (\text{A1})$$

The decision test is now defined as ($X' \leq \frac{\mathbb{H}_1}{\mathbb{H}_0} \gamma'$), where a user-specified false alarm rate (P_{FA}) determines the value of the threshold (γ') such that $P(X' < \gamma' | \mathbb{H}_0) \leq P_{FA}$.

2. Ballistic Imaging— K Points

The problem now is modified to describe an imaging scenario of scanning the FOV at a fixed square array of $(\sqrt{K} \times \sqrt{K})$ points. This results in a multiple hypothesis testing problem (K tests), where for large K it puts a lower bound on the SNR of the observation. To boost the SNR, one could use spatial aggregation by averaging over a number of observation points. This modifies the problem to averaging neighborhoods of points in an area measuring $\sqrt{W} \times \sqrt{W}$, $W < K$, effectively reducing the spatial resolution of the detection map (image). By decreasing the spatial resolution, this also decreases the variance at each point, modifying the decision test to

$$\mathbb{H}_0 : X' \sim \mathcal{N}\left(2\sqrt{NX_e + NX_s}, \frac{1}{W}\right),$$

$$\mathbb{H}_1 : X' \sim \mathcal{N}\left(2\sqrt{NX_e + NX_{s_{inc}}}, \frac{1}{W}\right). \quad (\text{A2})$$

This test is under the assumption that the averaging window will contain either no occluder points or all occluder points. In reality, the averaging filter will result in an observed point, $X'' \sim \mathcal{N}(\varphi E[X' | \mathbb{H}_0] + (1 - \varphi) E[X' | \mathbb{H}_1], 1/W)$, where φ is the fraction of the window containing nonoccluders, and E is the expected value operator. Our goal is to find the lower bound on the value of W that will guarantee an overall false alarm rate of less than P_{FA} , and we only consider the ideal case (all occluders or nonoccluders) in our calculations in order to obtain closed-form solutions.

The Bonferroni correction approach is a conservative method of controlling the false alarm rate for a detection problem under multiple independent and identically distributed tests [33]. The correction adjusts the threshold for each individual test in order to satisfy a lower (per test) false alarm rate

value (P_{FA}/K) such that each of the fixed number K points in the array (and W -point averaging filter) satisfies $[P(X < \gamma' | \mathbb{H}_0) \leq P_{FA}/K]$. With $\Phi(x)$ as the cumulative distribution function of the $\mathcal{N}(0, 1)$ density at the point x , this results in $[\gamma' \leq (1/\sqrt{W})\Phi^{-1}(P_{FA}/K) + 2\sqrt{NX_e + NX_s}]$. To give a satisfactory observation, we also bound the miss probability for detecting a ballistic photon by the same modified value (P_{FA}/K) such that $[P(X > \gamma' | \mathbb{H}_1) \leq P_{FA}/K]$. Using the miss bounds, we determine the lower bound on the necessary averaging window size (W) to image a fixed K -point array as

$$W \geq \left[\frac{1}{2} \frac{\Phi^{-1}\left(1 - \frac{P_{FA}}{K}\right) - \Phi^{-1}\left(\frac{P_{FA}}{K}\right)}{\sqrt{NX_e + NX_s} - \sqrt{NX_e + NX_{s_{inc}}}} \right]^2. \quad (\text{A3})$$

The minimum width of the occluding object (w_b) that can be reliably resolved for a given parameterized turbid medium can now be derived. Using the lower bound for W found in Eq. (A3), we can solve for the lower bound on the width using $w_b = \sqrt{(\text{FOV} \times W)/K}$.

3. Conventional Imaging Analysis

In the conventional imaging regime, there is no time-gating mechanism and all the photons that reach the detector over a long acquisition time will be observed [acquisition time $\gg (d/c) =$ direct line-of-sight flight time]. Therefore, a large number of photons sent through the medium will be collected by the detector. A problem occurs here, too—although the SNR is high due to the large number of photons, the average number of scattering events on each photon collected will

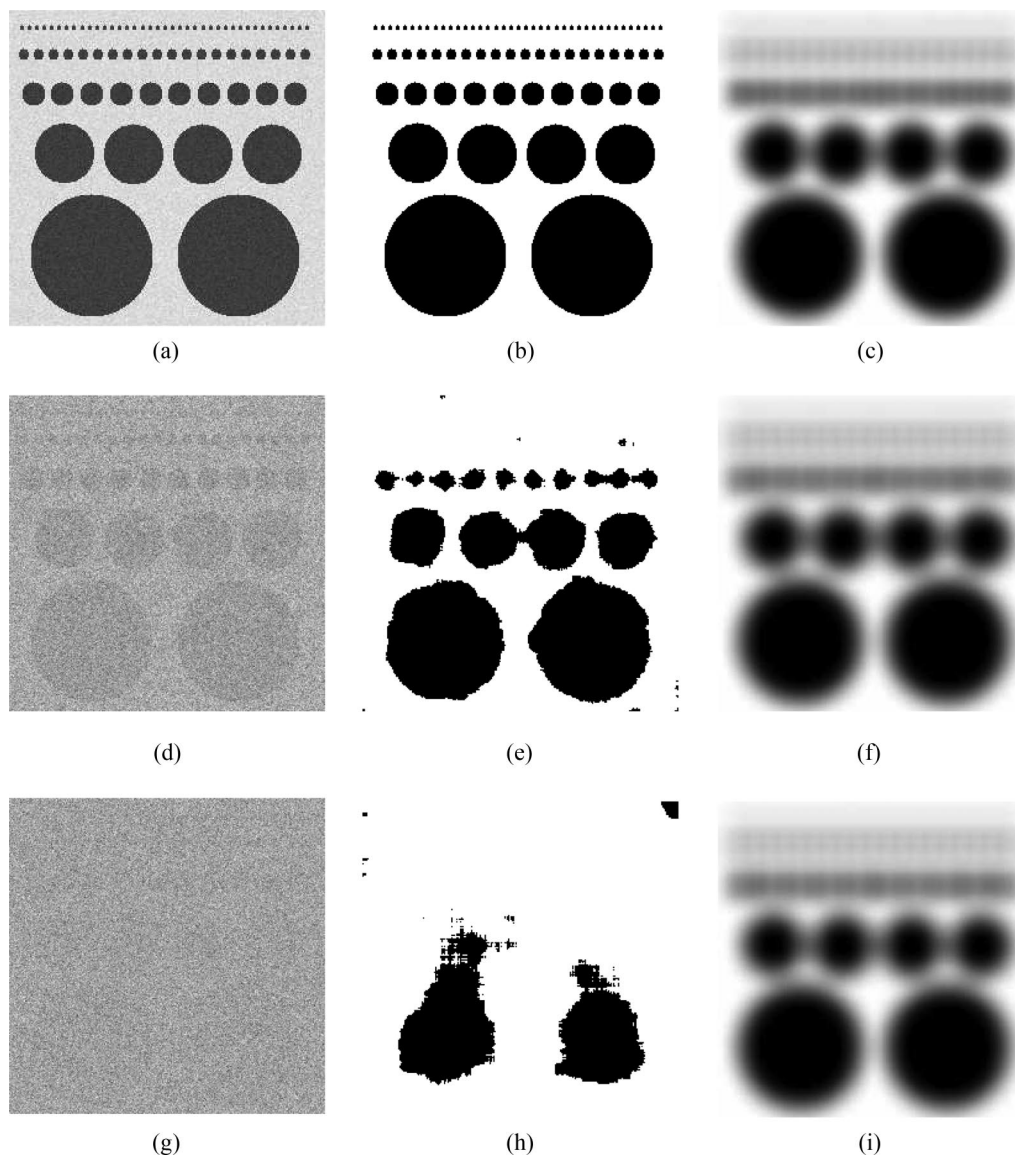


Fig. 17. Simulation experiments with $\text{FOV} = 50 \text{ m} \times 50 \text{ m}$, $d_{inc} = 0.3 \text{ m}$, and $\mu_t = 12.5^{-1} \text{ m}^{-1}$. (a)–(c) Ballistic, Bonferroni, and conventional observations at $d = 350 \text{ m}$, respectively. (d)–(f) Ballistic, Bonferroni, and conventional observations at $d = 400 \text{ m}$, respectively. (g)–(i) Ballistic, Bonferroni, and conventional observations at the critical distance $d = d_{critical} = 417 \text{ m}$, respectively.

also be high. As the number of scattering events increases for a photon, the spatial resolution of the occluding object will degrade. The lack of spatial information results in a blurred observation. Using random-walk theory [34,35], it is possible to solve for the minimum width of an occluding object that is reliably resolved using a conventional imaging system. The width [36] is found using the photon mean time of flight $\langle \Delta t \rangle$, which can be numerically computed as a function of the parameters of the medium (μ_s, μ_a). The modified minimum full width at half-maximum (FWHM) is equal to $w_{conv} = 0.94(\langle \Delta t \rangle c / \mu_s)^{1/2}$.

4. Optimal Resolution Trade-Offs

Ideally, one should choose the imaging system (ballistic or conventional) that reliably resolves the smallest possible object [$w = \min(w_{conv}, w_b)$]. The decision test using the minimum resolvable sizes derived above becomes

$$w_{conv} \underset{\text{ballistic}}{\overset{\text{conventional}}{\leq}} w_b \Rightarrow 0.94 \left(\frac{\langle \Delta t \rangle c}{\mu_s} \right)^{1/2} \underset{\text{ballistic}}{\overset{\text{conventional}}{\leq}} \sqrt{\frac{\text{FOV} \times W}{K}}. \quad (\text{A4})$$

Using the lower bound of W from Eq. (A3), one can solve for the critical distance ($d = d_{critical}$), the maximum distance at which ballistic still offers superior resolution relative to conventional imaging.

As an illustrative example, we considered a ballistic scanning experiment at ($K = 256^2$) points, imaging a $50 \text{ m} \times 50 \text{ m}$ FOV. The occluding objects were assumed to be circular of diameter 1.0, 2.0, 4.0, 10.0, and 20.0 m each of thickness $d_{inc} = 0.3 \text{ m}$ and $\mu_{inc} = 12.5 \text{ m}^{-1}$. We used false alarm rate $P_{FA} = 0.05$ and considered a heavy fog turbid medium with $\mu_t = 12.5^{-1} \text{ m}^{-1}$. Using the analysis from above, $d_{critical} = 417 \text{ m}$, which is consistent with earlier results we showed in Section 3. Figure 17 shows the effect of distance on the ballistic resolution, illustrating the captured ballistic and diffused (conventional) images at distances of $d = 350, 400, 417 \text{ m}$.

The authors wish to thank Ines Delfino, Heike Lischke, and Mohammad Alrubaiee for providing invaluable information and data throughout this project. This work was supported in part by Defense Advanced Research Projects Agency, Air Force Office of Scientific Research grant FA9550-06-1-0047. Approved for public release; distribution unlimited.

References

1. C. Dunsby and P. M. W. French, "Techniques for depth-resolved imaging through turbid media including coherence-gated imaging," *J. Phys. D* **36**, 207–227 (2003).
2. K. Yoo and R. R. Alfano, "Time-resolved coherent and incoherent components of forward light scattering in random media," *Opt. Lett.* **15**, 320–322 (1990).
3. A. F. Fercher, W. Drexler, C. K. Hitzenberger, and T. Lasser, "Optical coherence tomography—principles and applications," *Rep. Prog. Phys.* **66**, 239–303 (2003).
4. M. E. Zevallos, S. K. Gayen, M. Alrubaiee, and R. R. Alfano,

- "Time-gated backscattered ballistic light imaging of objects in turbid water," *Appl. Phys. Lett.* **86**, 0111151–0111153 (2005).
5. M. Paciaroni and M. Linne, "Single-shot, two-dimensional ballistic imaging through scattering media," *Appl. Opt.* **43**, 5100–5109 (2004).
6. D. Contini, F. Martelli, and G. Zaccanti, "Photon migration through a turbid slab described by a model based on diffusion approximation. I. Theory," *Appl. Opt.* **36**, 4587–4599 (1997).
7. I. Delfino, M. Lepore, and P. L. Indovina, "Experimental tests of different solutions to the diffusion equation for optical characterization of scattering media by time-resolved transmittance," *Appl. Opt.* **38**, 4228–4236 (1999).
8. W. Cai, S. K. Gayen, M. Xu, M. Zevallos, M. Alrubaiee, M. Lax, and R. R. Alfano, "Optical tomographic image reconstruction from ultrafast time-sliced transmission measurements," *Appl. Opt.* **38**, 4237–4246 (1999).
9. B. B. Das, F. Liu, and R. R. Alfano, "Time-resolved fluorescence and photon migration studies in biomedical and model random media," *Rep. Prog. Phys.* **60**, 227–292 (1997).
10. A. Gibson, J. Hebden, and S. Arridge, "Recent advances in diffuse optical imaging," *Phys. Med. Biol.* **50**, R1–R43 (2005).
11. H. Lischke, T. J. Loeffler, and A. Fischlin, "Aggregation of individual trees and patches in forest succession models: capturing variability with height structured, random, spatial distributions," *Theor. Popul. Biol.* **54**, 213–236 (1998).
12. S. V. Aert, D. V. Dyck, and A. J. den Dekker, "Resolution of coherent and incoherent imaging systems reconsidered—classical criteria and a statistical alternative," *Opt. Express* **14**, 3830–3839 (2006).
13. S. M. Kay, *Fundamentals of Statistical Signal Processing: Estimation Theory* (Prentice-Hall, 1993), Vol. 1.
14. L. L. Scharf, *Statistical Signal Processing: Detection, Estimation, and Time Series Analysis* (Addison-Wesley, 1991).
15. G. W. Sutton, "Fog hole boring with pulsed high-energy lasers—an exact solution including scattering and absorption," *Appl. Opt.* **17**, 3424–3430 (1978).
16. S. M. Kay, *Fundamentals of Statistical Signal Processing Detection Theory* (Prentice-Hall, 1998), Vol. 2.
17. M. Shahram and P. Milanfar, "Imaging below the diffraction limit: a statistical analysis," *IEEE Trans. Image Processing* **13**, 677–689 (2004).
18. A. Sommerfeld, *Optics Lectures on Theoretical Physics* (Academic, 1954), Vol. 4.
19. J. Goodman, *Introduction to Fourier Optics*, 3rd ed. (Roberts and Company, 2005).
20. G. B. Parrent, Jr. and B. J. Thompson, "On the Fraunhofer (far field) diffraction patterns of opaque and transparent objects with coherent background," *J. Mod. Opt.* **11**, 183–193 (1964).
21. D. N. Nikogosyan, "Beta barium borate (BBO)," *Appl. Phys. A* **52**, 359–368 (1991).
22. M. Ghotbi and M. Ebrahim-Zadeh, "Optical second harmonic generation properties of BiB_3O_6 ," *Opt. Express* **12**, 6002–6019 (2004).
23. E. Candès, J. Romberg, and T. Tao, "Stable signal recovery from incomplete and inaccurate measurements," *Commun. Pure Appl. Math.* **59**, 1207–1223 (2006).
24. J. Haupt and R. Nowak, "Signal reconstruction from noisy random projections," *IEEE Trans. Inf. Theory* **52**, 4036–4048 (2006).
25. R. Castro, J. Haupt, and R. Nowak, "Compressed sensing vs. active learning," in *2006 International Conference on Acoustics, Speech and Signal Processing* (IEEE, 2006), pp. 820–823.
26. D. Donoho, M. Elad, and V. Temlyakov, "Stable recovery of sparse overcomplete representations in the presence of noise," *IEEE Trans. Inf. Theory* **52**, 6–18 (2006).
27. M. Wakin, J. Laska, M. Duarte, D. Baron, S. Sarvotham, D.

- Takhar, K. Kelly, and R. Baraniuk, "An architecture for compressive imaging," in *2006 International Conference on Image Processing* (IEEE, 2006), pp. 1273–1276.
28. R. Castro, R. Willett, and R. Nowak, "Faster rates in regression via active learning," in *2005 Advances in Neural Information Processing Systems 18* (MIT Press, 2005), pp. 179–186.
 29. S. Farsiu, D. Robinson, M. Elad, and P. Milanfar, "Fast and robust multi-frame super-resolution," *IEEE Trans. Image Processing* **13**, 1327–1344 (2004).
 30. B. Eriksson and R. Nowak, "Maximum likelihood methods for time-resolved imaging through turbid media," in *2006 International Conference on Image Processing* (IEEE, 2006), pp. 641–644.
 31. S. Fantini, S. Walker, M. Franceschini, M. Kaschke, P. Schlag, and K. Moesta, "Assessment of the size, position, and optical properties of breast tumors *in vivo* by noninvasive optical methods," *Appl. Opt.* **37**, 1982–1989 (1998).
 32. F. Anscombe, "The transformation of Poisson, binomial and negative-binomial data," *Biometrika* **35**, 246–254 (1948).
 33. R. Miller, *Simultaneous Statistical Inference* (Springer, 1991).
 34. A. Gandjbakhche, G. Weiss, R. Bonner, and R. Nossal, "Photon path-length distributions for transmission through optically turbid slabs," *Phys. Rev. E* **48**, 810–818 (1993).
 35. A. Gandjbakhche, R. Nossal, and R. Bonner, "Resolution limits for optical transillumination of abnormalities deeply embedded in tissues," *Med. Phys.* **21**, 185–191 (1994).
 36. V. Chernomordik, R. Nossal, and A. Gandjbakhche, "Point spread functions of photons in time-resolved transillumination experiments using simple scaling arguments," *Med. Phys.* **23**, 1857–1861 (1996).